

Theoretical Study of Ethylene Hydroformylation on Atomically Dispersed Rh/Al₂O₃ Catalysts: Reaction Mechanism and Influence of the ReO_x Promoter

Seungyeon Lee, Abhirup Patra, Phillip Christopher, Dionisios G. Vlachos, and Stavros Caratzoulas*



Cite This: *ACS Catal.* 2021, 11, 9506–9518



Read Online

ACCESS |



Metrics & More



Article Recommendations

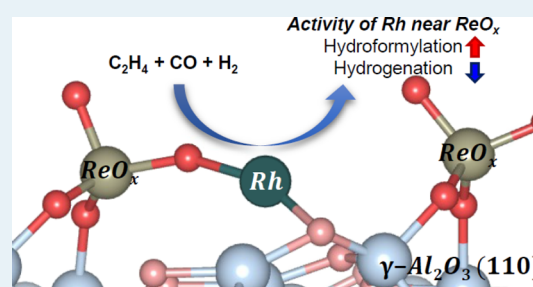


Supporting Information

ABSTRACT: Atomically dispersed late transition-metal catalysts on supports have demonstrated unexpectedly high activity and selectivity compared to metal clusters, attributed to the unique electronic properties determined by the metal–support interface and the presence of promoters that modify the local environment of the single-atom site. Through cooperativity and synergism, these structures provide a fertile ground for catalyst discovery. Understanding these materials at the atomic scale and how to tune their electronic properties will be key for designing novel catalysts for selective chemistries. Here, we use density functional theory calculations and first-principles microkinetic modeling to unveil extensive mechanistic knowledge about the cooperativity of atomically dispersed Rh–ReO_x pairs

on the γ -alumina support for the hydroformylation of ethylene to propanal. By considering a number of possible pre-catalyst complexes, we confirm that the most stable one is a Rh gem-dicarbonyl species, Rh(CO)₂, which, contrary to the homogeneous Wilkinson complex, assumes a 16-electron square-planar geometry by coordinating to two alumina surface oxygen atoms. We find the weakening of the Rh–CO coordinative bonds with increasing ReO_x loading, confirming an earlier experimental work. We develop mechanisms for two competing reactions, ethylene hydroformylation and hydrogenation, and show that they reproduce experimental observations and trends such as reaction kinetics and, most critically, the increase in hydroformylation selectivity in the presence of ReO_x. In these mechanisms, the catalyst is activated by the dissociation of one of the two CO ligands of Rh(CO)₂ to allow ethylene and H₂ coordination, in that order, and we provide evidence that H₂ dissociation on Rh is not oxidative. We determine the hydroformylation rate-limiting step and show that it depends on the local environment of Rh: in the absence of ReO_x, the hydroformylation is controlled by the acylation step and requires octahedrally coordinated Rh, namely, re-binding of a CO ligand prior to the acylation; in the presence of ReO_x, and owing to the weakening of the Rh–CO bonds, the requisite CO coordination prior to the insertion step becomes rate-controlling. We assert that ReO_x steers the reaction toward propanal by impeding a critical rearrangement of the Rh ligands that favors the competing reaction, ethylene hydrogenation.

KEYWORDS: hydroformylation, density-functional theory, single-atom catalysis, rhodium, heterogeneous, γ -alumina



1. INTRODUCTION

Combining the usually superior catalytic performance and/or selectivity of homogeneous catalysts with the stability, ease of separation, and reusability of heterogeneous catalysts is an emerging frontier in the field of catalysis and a goal long-sought. Advances in synthesis and characterization techniques now make possible the study of metal catalysts atomically dispersed on high-surface-area supports.^{1,2} Supported single-atom, late transition-metals have demonstrated uncharacteristically high catalytic activity and selectivity^{1,2} compared to their supported nanoparticle or nanocluster counterparts for a range of reactions.^{3–9} Their unique performance is attributed to the electronic properties of the typically cationic, atomically dispersed transition-metal and maximized metal–support interactions arising from the geometric confinement.^{1,10} The support functions as a proper ligand with a quasi-continuous spectrum of electronic states and properties quite different

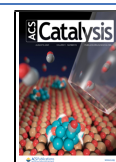
from those of molecular ligands in homogeneous systems. By altering the local environment of the dispersed atom, one can modulate its electronic behavior and thereby the activity and selectivity.

In a recent work, Lang et al.⁶ used the hydroformylation of ethylene as a model reaction to demonstrate that single-atom Rh supported on ZnO nanowires can rival Wilkinson's homogeneous catalyst in performance and selectivity. The hydroformylation of olefins is an important industrial process

Received: February 13, 2021

Revised: July 2, 2021

Published: July 15, 2021



in its own right as it is used to produce more than 10 million tons of aldehydes annually.¹¹ The reaction is almost exclusively catalyzed by homogeneous Rh and Co complexes, which, however, have inherent shortcomings such as cost-intensive recycling or catalyst leaching.^{10,11} There is, therefore, considerable motivation and interest for more robust catalytic solutions.

Using the same model reaction, Ro et al.¹² recently demonstrated that the reactivity of Rh atomically dispersed on γ -Al₂O₃ and its selectivity for propanal could be promoted by manipulating its local environment via the targeted deposition of Rh precursors near atomically dispersed ReO_x on γ -Al₂O₃. They further hypothesized that the high selectivity of atomically dispersed Rh–ReO_x pairs for propanal should be attributed to weaker Rh–CO binding on the ReO_x-modified support relative to the unmodified one. This was inferred from the blue shift in the CO stretching vibrations.

It is widely accepted that the homogeneous hydroformylation reaction on Co or Rh catalysts follows the Heck–Breslow mechanism,¹³ which has been extensively tested experimentally and theoretically.^{14–16} Despite that, there is lack of consensus across studies about the rate-limiting step of the reaction as it strongly depends on the catalyst, the reaction conditions, and the olefin. Heck and Breslow originally proposed that, on [HCo(CO)₄], the turnover rate is controlled by the H₂ oxidative addition.¹³ This was challenged by subsequent quantum chemical calculations.^{17–21} Huo et al.¹⁷ proposed that the H₂ coordination to Co is rate-limiting, but a study at the CCSD(T) theory level by Rush et al.¹⁸ suggested the olefin coordination instead, due to the very low concentration of the coordinatively unsaturated complex [HRh(CO)₃]. Jacobs et al.²¹ and Decker and Cundari²⁰ investigated the full catalytic cycle for phosphine-modified Rh catalysts, [HRh(CO)₃(PPh₃)], [HRh(CO)₂(PPh₃)₂],²¹ and [HRh(Ph₃)₂(CO)]²⁰ complexes and, respectively, proposed the hydrometalation (viz. olefin insertion to the metal–hydrogen bond) and the acylation (viz. CO insertion to the metal–alkyl bond) as rate-controlling. Another layer of complexity was revealed by Sparta et al.,²² who investigated the effect of ligands of varying electron-withdrawing ability and demonstrated that, as the ligands become more electron-withdrawing, the rate-limiting step shifts from the olefin coordination/hydrometalation to the reductive elimination of the aldehyde. According to Sparta et al.,²² ligands that are stronger π -acceptors than phosphines reduce the energy barrier for olefin coordination/hydrometalation. In the Heck–Breslow homogeneous catalytic cycle, the reaction kinetics is intimately connected with the resting state of the catalyst as well as the rate-limiting step.^{10,14} The reaction follows first-order kinetics in the olefin concentration and an inverse first-order in the CO partial pressure when the resting state of the catalyst is the pre-catalyst complex [HRh(L)₂(CO)₂], and the rate is controlled either by the olefin coordination or hydrometalation. If the catalyst's resting state is the [(Acyl)Rh(L)₂(CO)] complex, the reaction is first-order in the H₂ partial pressure, and the rate is controlled by the H₂ oxidative addition.

The catalytic activity of Rh or Co catalysts for ethylene hydroformylation has been explored in heterogeneous catalysis as well. Navidi et al.²³ studied the reaction on 5%Rh/Al₂O₃, 1%Co/Al₂O₃, and 0.5%Co–0.5%Rh/Al₂O₃ catalysts and reported that finely dispersed Rh and Co particles were the most active and selective (up to 45%) in hydroformylation to propanal and propanol. In a subsequent kinetic study, Navidi

et al.²⁴ regressed a single-event microkinetic model to experimental data and proposed the CO insertion as a kinetically relevant step. Xie et al.²⁵ have leveraged the catalytic activity of RhCo bimetallics for ethylene hydroformylation to synthesize C3 oxygenates (propanal and 1-propanol) on RhCo_x/MCM-41 by coupling to CO₂-assisted ethane dehydrogenation and reforming over the Fe₃Ni₁/CeO₂ catalyst. The CoRh bimetallic has also been investigated by Huang et al.,²⁶ who reported that adding Co to the Rh-based catalyst increased the selectivity for ethylene hydroformylation. By performing density functional theory (DFT) calculations on Rh(111) and CoRh(111), they proposed the CO insertion as the hydroformylation rate-limiting step. Wang et al.²⁷ have shown that CoO-supported Rh single-site catalysts are remarkably active and selective (94.4%) for propene hydroformylation. Using the DFT calculations in which Rh was doped into the surface of the oxide, they proposed that the aldehyde elimination is rate controlling. In other works, Liu et al.²⁸ demonstrated by means of DFT calculations that Rh₂P(111) would significantly enhance the styrene hydroformylation activity in comparison with Rh, which was further confirmed by experiments. Their calculations also suggested that the product elimination is rate determining.

The heterogeneous catalytic cycle on supported, atomically dispersed transition metals is less studied and understood. In recent works, Amsler et al.²⁹ calculated the energetics of hydroformylation over atomically dispersed [HRh(CO)₃] on the CeO₂ support. The study considered the Heck–Breslow mechanism alone and concluded that the rate-limiting step is the CO insertion.

In this paper, we study the hydroformylation and hydrogenation of ethylene over atomically dispersed Rh–ReO_x/Al₂O₃ as a prime example of a promoter's (ReO_x) ability to modify the local environment of the single-atom site (Rh) and influence the selectivity of the catalyst. Using DFT calculations and microkinetic modeling, we unveil extensive mechanistic knowledge about the cooperativity and synergism of the atomically dispersed Rh–ReO_x pairs and provide answers to a number of outstanding questions.

The paper is structured as follows: first, we establish that Rh(CO)₂ is the most stable pre-catalyst complex, which assumes a 16-electron, square-planar geometry that also engages two surface O atoms as ligands. Next, we undertake a detailed analysis of the electronic and vibrational properties of the Rh gem-dicarbonyl species and examine the influence of ReO_x and of surface hydroxylation. We show the weakening of the Rh–CO coordinative bonds with increasing ReO_x loading and demonstrate an attendant blue shift in the CO's stretching vibrations on dry γ -Al₂O₃. Importantly, we caution that this correlation is not generally true as we demonstrate that it does not hold for the hydroxylated support. Finally, we undertake a comprehensive mechanistic study of the two competing reactions, ethylene hydroformylation and hydrogenation, and validate the proposed mechanisms by extensive microkinetic analysis which shows that they can reproduce experimental¹² observations and trends such as reaction kinetics; apparent activation energies for the two competing pathways and relationships between them; and, most critically, the increase in propanal selectivity in the presence of ReO_x. We also show that the hydroformylation rate-limiting step depends on the local environment of the Rh site. According to our analysis, ReO_x increases the selectivity for propanal by sterically impeding the most dominant hydrogenation pathway while

shifting the propanal production rate-limiting step from the CO insertion to the CO coordination. This work provides an in-depth understanding of the correlation between the electronic environment of atomically dispersed Rh and the catalytic activity.

2. METHODS

2.1. γ -Al₂O₃ Model Surfaces. For the support surfaces, we considered the most exposed (110) facet of nonspinel γ -Al₂O₃.^{30–32} As the (110) termination retains some degree of hydroxylation even at high temperatures (>1000 K),³³ we examined both anhydrous and hydrated (coverage of 5.9 OH/nm²) surfaces. Following prior works, the ReO_x-modified surfaces were modeled by depositing perrenic acid (HReO₄) in a dissociated form.^{12,34} Hereinafter, the ReO_x-modified surfaces will be referred to as n ReO₄-Al₂O₃ or n ReO₄·[Al₂O₃·H₂O], depending on whether the surface is anhydrous or not, where n denotes the Re loading (0, 1 or 2.9 wt %). The surface Rh atom was added in its metallic state, maintaining electroneutrality (hereinafter, Rh/ n ReO₄-Al₂O₃ or Rh/ n ReO₄·[Al₂O₃·H₂O]).

2.2. DFT Calculations. In the surface characterization periodic DFT calculations presented in Section 3.1, the γ -Al₂O₃(110) surface was represented by a four-layer (bottom layer fixed) 2 × 2 slab separated by its periodic image in the z -direction by a vacuum region of 15 Å; the physical dimensions of the 2 × 2 slab were 16.66 × 16.02 × 20 Å. In the mechanistic studies presented in Section 3.2, the γ -Al₂O₃(110) surface was represented by a four-layer (bottom layer fixed) 1 × 2 slab separated by its periodic image by a vacuum region of 15 Å; the physical dimensions of the 1 × 2 slab were 8.33 × 16.02 × 20 Å.

Spin-polarized periodic DFT calculations were performed at the Perdew–Burke–Ernzerhof (PBE)³⁵ theory level with a D3 dispersion (zero damping) of Grimme et al.³⁶ and dipole corrections. The projector-augmented wave^{37,38} method was used to model core electrons. Conventional valence configurations were employed for all elements with the exception of Rh for which the semicore p -states were also included in the valence shell (“Rh_pv” in VASP). For all structures, an energy cutoff of 400 eV (600 eV for bulk) was used. The Brillouin zone was sampled on (3 × 3 × 1) and (4 × 2 × 1) k -point grids for the characterization and mechanistic studies, respectively. A Gaussian smearing of 0.1 eV width was used. The SCF iterations were converged to 10^{−6} and 10^{−4} eV for bulk and slab calculations, respectively. Geometries were optimized to 0.01 and 0.05 eV/Å for bulk and slab calculations, respectively. Transition states were located by the climbing-image NEB method,^{39,40} converged to 0.05 eV/Å (10^{−6} eV for the SCF loop calculations), and confirmed by vibrational frequency analysis. All DFT calculations were performed with the Vienna ab initio simulation package (VASP, version 5.4.1).^{41,42} Bader charge analysis⁴³ was performed using the Henkelman et al. implementation.⁴⁴

It is essential to briefly discuss the accuracy of the PBE functional in relation to the computed pathways and kinetic parameters. On average, the PBE functional, such as most GGA functionals, underestimates reaction barriers by 6–7 kcal/mol,^{45–47} which is a lot better than the 10–20 kcal/mol error of LDA but still not close to the desired chemical accuracy of 1 kcal/mol. On the upside, GGA functionals generally predict transition complex geometries in good agreement with post-Hartree–Fock correlation methods.^{48,49}

For the main group elements and for molecule–surface interactions, meta-GGA functionals, such as TPSS and SCAN, provide better molecular properties than the GGA functionals. However, their performance is not too different from GGAs—with the exception of the revised-TPSS (RTPSS), which performs exceptionally well with the BH6 data set for activation barriers.⁵⁰ On the other hand, for a larger data set like SBH10⁴⁵ and for oxide surfaces,^{47,50} more accurate activation barriers have been achieved by adding the Grimme’s D3 dispersion correction to the PBE functional, which is the approach taken in this work. The screened hybrid functionals HSE and RPA can provide a reasonably good description of activation barriers for small-molecule dissociation. However, these approximations are computationally too expensive for the purposes of our study.

2.3. Microkinetic Modeling. Microkinetic modeling was performed using CHEMKIN.⁵¹ All kinetic parameters were obtained from the DFT calculations, as described in Section 3.2. The thermal corrections to the electronic energies were obtained within the harmonic oscillator approximation using the Python Multiscale Thermochemistry Toolbox (pMuTT).⁵² Reaction conditions were chosen to match those in experiments:¹² 393–443 K, atmospheric pressure, a reactant gas mixture of C₂H₄, H₂, and CO at a molar ratio of 1:1:1, and a total flow rate of 30 cm³ (STP) min^{−1}. All microkinetic model parameters and results are provided in Section S1.

3. RESULTS

3.1. Active Site Characterization. For the reference state of the catalyst (pre-catalyst complex), we sampled and relaxed on the support numerous possible coordination complexes of Rh with CO, H, and H₂ ligands. We retained the square-planar Rh(CO)₂ configuration as it was the one of the lowest energy. The trigonal pyramidal complexes of [HRh(CO)₂] or [Rh(CO)₃], analogous to the homogeneous pre-catalyst complexes proposed by Wilkinson and by Heck and Breslow,¹⁰ were found to be less stable than Rh(CO)₂ by 0.4 eV or more (Table S2.1).

We are interested in understanding how ReO_x affects the strength of CO binding to Rh and how the latter is related to the electronic modification of the surface and the electronic structure of the putative Rh–ReO_x pairs. Ro et al.¹² have hypothesized that the blue shift in the dicarbonyl antisymmetric stretch with increasing ReO_x loading is due to the weaker Rh–CO binding and reasoned that ReO_x, a strong Lewis acid, withdraws electron density from the neighboring Rh atom, making it more cationic and thereby a weaker π -donor.¹² We investigate these hypotheses for dry and partially hydrated γ -Al₂O₃(110) at 0, 1.0, and 2.9 wt % ReO_x loadings. For each system, among an extensive set of configurations of Rh, ReO_x, and Rh–ReO_x on the support, we retained for further study the one of the lowest energy (see Section S2 for more details).

3.1.1. Rh/ n ReO₄-Al₂O₃(110). On the dry (110) surface of alumina, Rh coordinates to two oxygen atoms, however, to which of the two depends on whether the surface is ReO_x-modified: in the absence of ReO_x, Rh coordinates to two surface O atoms, but on the ReO_x-modified surface, Rh relocates and accepts ReO_x as a ligand, forming a Rh–O–Re linkage (Figure 1c). Bader analysis prior to CO binding shows that Rh on ReO₄-Al₂O₃(110) loses some electron density (0.12e) relative to Rh/Al₂O₃(110) as its partial charge changes from −0.08e to 0.04e (Table 1). A second ReO_x molecule in

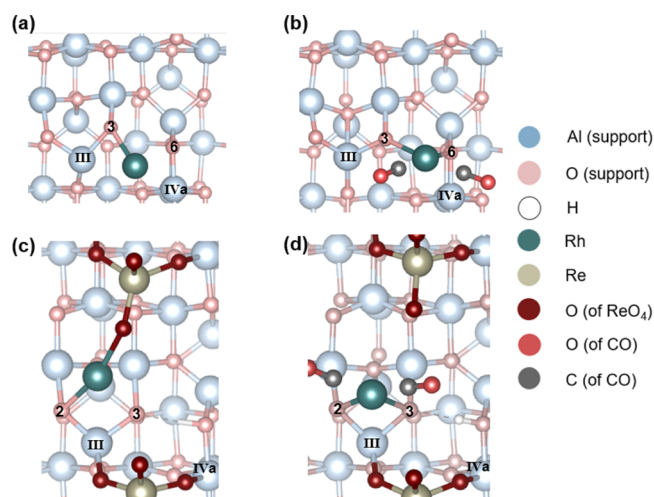


Figure 1. Equilibrium geometries on $\text{Al}_2\text{O}_3(110)$. (a) $\text{Rh}/\text{Al}_2\text{O}_3(110)$; (b) $\text{Rh}(\text{CO})_2/\text{Al}_2\text{O}_3(110)$; (c) $\text{Rh}/\text{ReO}_4\text{-Al}_2\text{O}_3(110)$; and (d) $\text{Rh}(\text{CO})_2/\text{ReO}_4\text{-Al}_2\text{O}_3(110)$. Rh nearest-neighbor surface oxygen atoms labeled according to the scheme in Figure S2.1.

the simulation supercell (corresponding to ReO_x loading of $n = 2.9$ wt %) has the opposite effect, albeit small: Rh gains 0.03e of electron density relative to $n = 1$. Therefore, overall, the Bader charge values indicate that Rh experiences a scant re-distribution of its electron density in the presence of ReO_x , and remains in the metallic state despite the adjacent, strongly Lewis acidic ReO_x . Rh also presents a magnetic moment of $\sim 1 \mu_B$, which is consistent with the d^8s^1 metallic state. On the other hand, ReO_x withdraws the electron density from the alumina support (see Table 1), suggesting it is partially reduced. This interpretation is corroborated by analysis of the Re-induced density of states in $\text{Rh}/\text{ReO}_4\text{-Al}_2\text{O}_3(110)$, where new orbitals appear below the Fermi level that are absent from the Re-PDOS of $\text{ReO}_4\text{-Al}_2\text{O}_3(110)$ (no Rh on the surface) (Figure S3.1). Evidently, in the presence of Rh, ReO_x is reduced more readily and this appears to be consistent with previous reports.⁵³ ReO_x seems to have one more notable effect on the electronic state of the system: the Fermi level in $\text{Rh}/2.9\text{ReO}_4\text{-Al}_2\text{O}_3(110)$ is 0.23 eV lower than in $\text{Rh}/\text{Al}_2\text{O}_3(110)$, with a concomitant drop in the spin-polarized d-bands of Rh (by 0.28 and 0.36 eV for the spin-up and spin-down bands, respectively).

Upon CO binding, the Rh-O-Re linkage breaks (cf. Figure 1c,d), Rh is again coordinated to two O atoms of the support and assumes a slightly distorted planar coordination geometry; the ReO_x modifier remains in the vicinity of one of its O atoms coordinated to an Al_{III} site. There is a substantial change in the CO binding energy with ReO_x loading. The formation of the $\text{Rh}(\text{CO})_2$ species is exergonic by 5.4 eV on the unmodified

surface, but this energy drops to 4.2 and 3.8 eV on $\text{Rh}/\text{ReO}_4\text{-Al}_2\text{O}_3(110)$ and $\text{Rh}/2.9\text{ReO}_4\text{-Al}_2\text{O}_3(110)$, respectively. A blue shift in the CO stretching vibrations is also predicted (Figure 2b), which agrees with the Fourier transform infrared studies of Ro et al.¹² The blue shift in the IR spectra suggests a weaker Rh-to-CO π -donation, which is in line with the aforementioned shift in Rh's d-band to lower energies with increasing ReO_x loading. Indeed, post-CO-binding Bader analysis confirms that CO loses some electron density with increasing ReO_x loading, with a total change of +0.06e in going from $\text{Rh}(\text{CO})_2/\text{Al}_2\text{O}_3(110)$ to $\text{Rh}(\text{CO})_2/2.9\text{ReO}_4\text{-Al}_2\text{O}_3(110)$.

Remarkably, when CO binds to $\text{Rh}/\text{Al}_2\text{O}_3(110)$, the electron density of Rh undergoes substantial re-distribution, as indicated by a jump in its partial charge from $-0.08e$ to $+0.64e$. This lost charge of 0.72e is not transferred to the bound CO molecules, whose partial charges add up to only $-0.10e$. In fact, most of the electron density lost by Rh is delocalized over the alumina support, which gains 0.54e of electron density (Table 1). Furthermore, the +0.72e bounce in the partial charge strongly suggests that Rh undergoes oxidation. This also seems consistent with its magnetic moment, which changes from ~ 1 , prior to $(\text{CO})_2$ binding, to $0 \mu_B$.

The electronic interactions related to the oxidation of Rh can be understood as follows. Figure 3a shows the s-band of Rh and Figure 3b shows the surface Al- and O-projected densities of states (PDOSs) in the equilibrium geometry of $\text{Rh}(\text{CO})_2/\text{Al}_2\text{O}_3(110)$ but with the dicarbonyl complex isolated out of the system (and fixed in its equilibrium geometry in $\text{Rh}(\text{CO})_2/\text{Al}_2\text{O}_3(110)$). In other words, we are reconstructing $\text{Rh}(\text{CO})_2/\text{Al}_2\text{O}_3(110)$ in stages and consider the catalyst, $\text{Rh}/\text{Al}_2\text{O}_3(110)$, in the configuration that it will finally have after CO binding. This is important because, as mentioned earlier, CO binding induces the rearrangement of Rh and ReO_x on the surface. The peak at the Fermi level and the one just above the Fermi level in the Rh s-band (Figure 3a) correspond to two non-degenerate s-orbitals, one occupied and the other empty. On account of the square-planar geometry of $\text{Rh}(\text{CO})_2$ on $\text{Al}_2\text{O}_3(110)$, the isolated dicarbonyl complex possesses a C_{2v} symmetry and will interact with the s-band of Rh through its HOMO -1 , which is of appropriate A_1 symmetry; the orbitals of $(\text{CO})_2$ along with their irreducible representations are shown in Figure 4. Upon $(\text{CO})_2$ coordination, the mixing of the HOMO -1 of $(\text{CO})_2$ with the Rh s-orbital at the Fermi level is a two-orbital three-electron interaction whose anti-bonding combination lies above the Fermi level. As a result, this anti-bonding orbital (mostly of Rh character) empties its electron at the Fermi level into orbitals that are localized on Al and O atoms of the support; the latter are shown in Figure 3b prior to the $(\text{CO})_2$ coordination.^{54–56} This picture is consistent with the Bader

Table 1. Bader Partial Charges of Rh, CO, HReO_4 , and Al_2O_3 for Rh and $\text{Rh}(\text{CO})_2$ on $\gamma\text{-Al}_2\text{O}_3$

surface	Re loading (wt %)	$\text{Rh}/\text{Al}_2\text{O}_3$			$\text{Rh}(\text{CO})_2/\text{Al}_2\text{O}_3$			
		Rh	HReO_4	Al_2O_3	Rh	2CO	HReO_4	Al_2O_3
$\text{Al}_2\text{O}_3(110)$	0	−0.08		0.08	0.64	−0.10		−0.54
	1	0.04	−0.48	0.44	0.62	−0.08	−0.27	−0.27
	2.9	0.01	−0.39, −0.24	0.63	0.60	−0.04	−0.24, −0.36	0.03
$[\text{Al}_2\text{O}_3 \cdot \text{H}_2\text{O}](110)$	0	0.05		−0.05	0.63	−0.12		−0.51
	1	0.33	−0.73	0.39	0.42	−0.22	−0.52	0.32
	2.9	0.32	−0.74, −0.23	0.64	0.41	−0.27	−0.51, −0.22	0.58

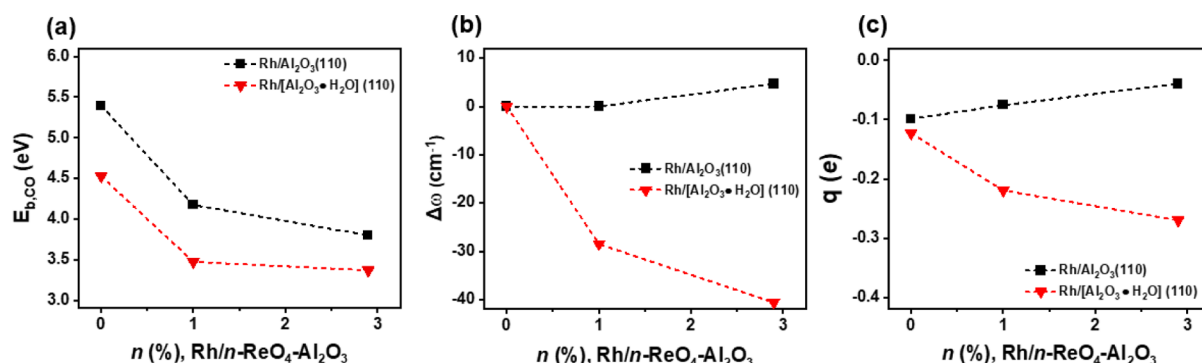


Figure 2. Plots as a function of ReO_4 loading, n , of (a) CO binding energy to Rh, $E_{b,CO}$; (b) dicarbonyl antisymmetric vibrational frequency shift, $\Delta\omega$, with respect to the surface without the ReO_4 modifier; and (c) total Bader partial charge, q , on dicarbonyl species. Systems shown are $\text{Rh}/n\text{ReO}_4\text{-Al}_2\text{O}_3(110)$ and $\text{Rh}/n\text{ReO}_4\text{-[Al}_2\text{O}_3\cdot\text{H}_2\text{O]}(110)$. (Dicarbonyl frequencies are reported in Table S4.1.)

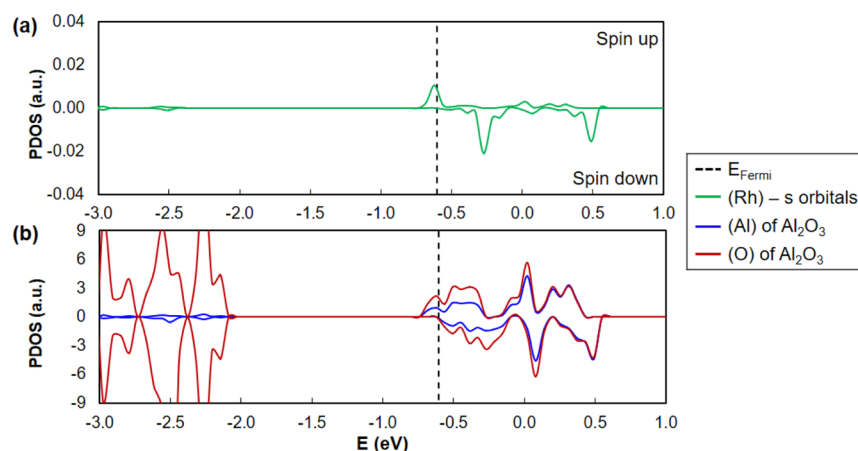


Figure 3. (a) Rh s-band in $\text{Rh}/\text{Al}_2\text{O}_3(110)$ in the equilibrium geometry of $\text{Rh}(\text{CO})_2/\text{Al}_2\text{O}_3(110)$, namely, with CO isolated out of the system. (b) Al- and O-projected densities of states for the same system as in (a). (Vertical dotted lines indicate Fermi energies.)

analysis we described earlier and which showed an overall increase in the electron density of the support. Evidently, Rh is oxidized by the support but only because the CO coordination induces Rh relocation on the surface, which brings the Fermi level into the conduction band of Al_2O_3 . Indeed, Figure 5 compares the surface Al and O PDOSs for fully relaxed $\text{Rh}/\text{Al}_2\text{O}_3(110)$, namely, before the CO coordination to Rh and for fully relaxed $\text{Rh}(\text{CO})_2/\text{Al}_2\text{O}_3(110)$. Prior to CO binding, the Fermi level is within the band gap, at -1.18 eV (Figure 5a). After CO binding, the Fermi level is shifted up into the conduction band of the support, at -0.61 eV (Figure 5b); the newly occupied states at the Fermi level correspond to the surface Al and O states over which the Rh electron is delocalized.

A similar behavior is observed for CO binding to Rh on the ReO_x -modified surfaces. The partial charge on Rh is practically unchanged with ReO_x loading [$+0.62$ and $+0.60$ e in $\text{Rh}(\text{CO})_2/1.0\text{ReO}_4\text{-Al}_2\text{O}_3(110)$ and $\text{Rh}(\text{CO})_2/2.9\text{ReO}_4\text{-Al}_2\text{O}_3(110)$, respectively], which means that ReO_x does not make Rh more cationic, as hypothesized in an earlier experimental work.¹² Furthermore, there is again a change in the magnetic moment of Rh, from $\sim 1 \mu_B$, prior to CO binding, to $0 \mu_B$, which indicates the oxidation to the $+1$ state. Figure S3.2 shows the s-band of Rh in the equilibrium geometry of $\text{Rh}(\text{CO})_2/2.9\text{ReO}_x\text{-Al}_2\text{O}_3(110)$ but with the dicarbonyl complex isolated out of the system. We see again the two non-degenerate peaks just below and above the Fermi level. In a similar fashion to

$\text{Rh}(\text{CO})_2/\text{Al}_2\text{O}_3(110)$, the interaction between the HOMO -1 of CO and the occupied Rh s-orbital at the Fermi level generates an anti-bonding state that empties its electron at the Fermi level.

One notable difference between the Al_2O_3 and $\text{ReO}_x\text{-Al}_2\text{O}_3$ surfaces, however, is how Rh's lost electron density is redistributed over the support and ReO_x at varying ReO_x loadings. In the case of $\text{Rh}(\text{CO})_2/\text{ReO}_4\text{-Al}_2\text{O}_3(110)$, ~ 0.3 of the ~ 0.6 e lost by Rh is gained by the alumina support and the remaining ~ 0.3 e is gained by ReO_x . At higher ReO_x loadings ($\text{Rh}(\text{CO})_2/2.9\text{ReO}_4\text{-Al}_2\text{O}_3(110)$), almost all of Rh's lost charge is shared between the ReO_x molecules in the vicinity of Rh (see Table 1); this makes sense given that ReO_4 is more reducible than Al_2O_3 .^{57,58} The preferential charge transfer into ReO_4 is also reflected in the DOS of $\text{Rh}(\text{CO})_2/\text{ReO}_4\text{-Al}_2\text{O}_3(110)$. Figure S3.3 shows the DOS of $\text{Rh}(\text{CO})_2/2.9\text{ReO}_4\text{-Al}_2\text{O}_3(110)$ projected onto the ReO_4 , Al, and O atoms of the support. Comparing with Figure S3.2b, we see that the states at the Fermi level, into which the aforementioned Rh-dicarbonyl anti-bonding orbital combinations empty their electrons, are now mostly Re states.

These findings are consistent with recent X-ray photoelectron spectroscopy measurements of atomically dispersed Rh on ZnO nanowires by Lang et al.⁶ After reduction with H_2 , the metallic Rh acquired a positive charge upon formation of the $\text{Rh}(\text{CO})_2$ gem-dicarbonyl species, while the ZnO support

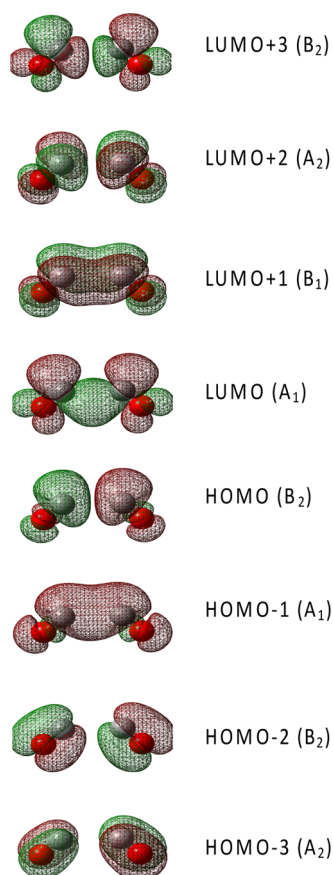


Figure 4. Gas-phase, C_{2v} molecular orbitals of dicarbonyl (CO)₂ in the Rh-bound geometry. Orbital symmetries are shown in parentheses.

was partially reduced. Similar observations have been made for $\text{Rh}(\text{CO})_2$ on SiO_2 and Al_2O_3 supports.^{59,60}

These electronic changes are directly related to the dynamics of CO binding. As we mentioned earlier, CO binding to Rh results in the rearrangement of the Rh and ReO_x on the surface of the support and in possible minor surface reconstruction. The associated distortion energy is already incorporated in the

$\text{Rh}(\text{CO})_2$ binding energies shown in Figure 2a because they are referenced to the equilibrium geometry of the catalyst. Energy decomposition analysis, whereby the CO binding energies are referenced to the respective distorted geometries (viz. the equilibrium geometries after CO binding), yields the distortion energy values of 0.1, 0.7, and 0.7 eV for the coordination of a single CO molecule and 0.4, 1.4, and 1.7 eV for the coordination of two CO molecules to $\text{Rh}/n\text{ReO}_4\text{-Al}_2\text{O}_3(110)$, $n = 0, 1, 2.9$, respectively. This surface distortion energy must be expended as the CO molecule approaches Rh from the gas phase and, although some of it will be recovered (owing to the attractive Rh–CO forces), it does indicate that the CO coordination is an activated process. Due to the large number of nuclear degrees of freedom involved in the surface reconstruction in the course of CO binding, NEB calculations failed to converge and thus we were unable to isolate a transition state and estimate the CO coordination energy barrier. Nevertheless, it is quite evident that the CO coordination to Rh is dynamically a lot easier in the absence rather than in the presence of ReO_x .

The rearrangement of the surface Rh and ReO_4 due to CO binding has a great effect on the Rh d-band. To see this, in Figure 6, we compare the Rh d-bands of four different systems: (a) $\text{Rh}/\text{Al}_2\text{O}_3(110)$ in its equilibrium geometry; (b) $\text{Rh}/\text{Al}_2\text{O}_3(110)$ fixed in the equilibrium geometry of $\text{Rh}(\text{CO})_2/\text{Al}_2\text{O}_3(110)$ (viz., CO is removed from the system); (c) $\text{Rh}/2.9\text{ReO}_4\text{-Al}_2\text{O}_3(110)$ in its equilibrium geometry; and (d) $\text{Rh}/2.9\text{ReO}_4\text{-Al}_2\text{O}_3(110)$ fixed in the equilibrium geometry of $\text{Rh}(\text{CO})_2/2.9\text{ReO}_4\text{-Al}_2\text{O}_3(110)$. In other words, (b,d) are the restructured geometries that will result upon binding of the two CO ligands and the formation of the $\text{Rh}(\text{CO})_2$ species. With regard to the systems in their respective equilibrium geometries, we noted earlier that the Fermi level in system (c) is 0.23 eV lower than in system (a), with a concomitant drop in the spin-polarized d-bands of Rh (by 0.28 and 0.36 eV for the spin-up and spin-down bands, respectively). With regard to the restructured, out-of-equilibrium systems (b,d), we see that both in the absence and presence of the ReO_4 promoter, Rh d-orbitals appear at the Fermi level (Figure 6c,d); the Fermi level is at -0.61 and -0.73 eV, respectively. These Rh d-orbitals are in essence anti-bonding molecular orbitals between the Rh atom and the two surface O atoms to which it is coordinated.

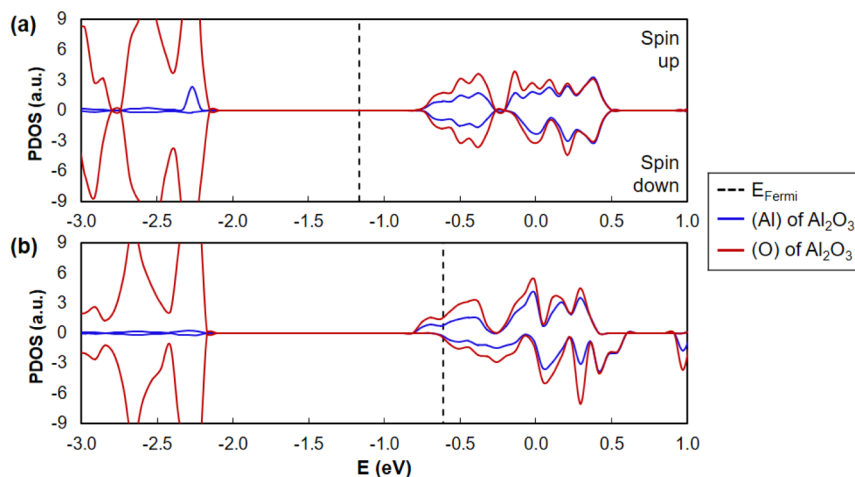


Figure 5. (a) Surface Al and O PDOSs for $\text{Rh}/\text{Al}_2\text{O}_3(110)$ in its equilibrium geometry (viz. before the formation of the Rh-dicarbonyl species). (b) Surface Al and O PDOSs for $\text{Rh}(\text{CO})_2/\text{Al}_2\text{O}_3(110)$ in its equilibrium geometry (viz. after the formation of the Rh-dicarbonyl species). (Vertical dotted lines indicate Fermi energies after the realignment of the vacuum levels with (a) as the reference.)

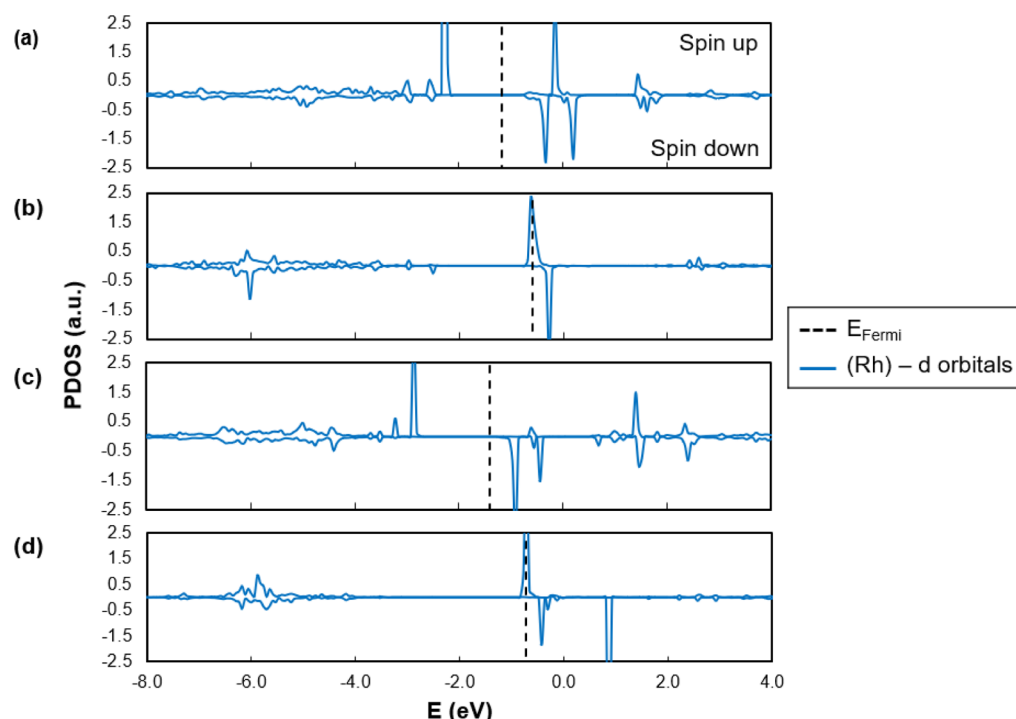


Figure 6. Rh PDOS for (a) Rh/Al₂O₃(110) in its equilibrium geometry, (b) Rh/Al₂O₃(110) fixed in the equilibrium geometry of Rh(CO)₂/Al₂O₃(110) (viz., CO is removed from the system), (c) Rh/2.9ReO₄-Al₂O₃(110) in its equilibrium geometry, and (d) Rh/2.9ReO₄-Al₂O₃(110) fixed in the equilibrium geometry of Rh(CO)₂/2.9ReO₄-Al₂O₃(110). (Vertical dotted lines indicate Fermi energies after the realignment of the vacuum levels with (a) as the reference.)

They are mostly of metal d character (of *xy*, *yz*, and maybe *xy* symmetries, depending on the orientation of the (RhOO) plane with respect to the surface) and participate in π back-donation upon CO binding. Owing to their lying lower in system (d) than in system (b), we expect a weaker π back-donation in (d) than in (b), which, once again, is consistent with the blue-shifting of the CO stretching vibrations with ReO_x loading.

Therefore, the presence of ReO_x has two related effects: it weakens the bonding in the Rh-(CO)₂ surface species, by diminishing the binding effect of metal-to-ligand π back-donation, but it also kinetically impedes their formation.

3.1.2. Rh/*n*ReO₄-[Al₂O₃·H₂O](110). The hydroxylated Al₂O₃(110) surface behaves differently from the anhydrous one. The most salient differences revealed by our simulations are the following:

- For all three ReO₄ loadings, *n* = 0, 1, and 2.9 wt %, the CO binds to Rh more weakly relative to the corresponding anhydrous surfaces (by 0.9, 0.7, and 0.4 eV, respectively).
- Although the Rh-CO binding strength is diminished with ReO₄ loading, Rh's ability to be a π -donor appears to be enhanced. This is clearly manifested in the total partial charge on the two CO molecules, which becomes increasingly negative with ReO_x loading [−0.12, −0.22, and −0.27e for *n* = 0, 1, and 2.9 wt %, respectively] (Table 1), and in response to which the stretching vibrations are red-shifted by about 30 and 40 cm^{−1} for *n* = 1 and *n* = 2.9 wt % relative to the unmodified surface (Rh/[Al₂O₃·H₂O](110)) (Table S4.1). This is in contrast with the experimental observations of Ro et al.¹² It is instructional to identify the reasons behind this very different behavior. The coordination geometry of

Rh is not affected by the presence of hydroxyl groups on the surface of the support—it remains square-planar, defined by the two surface oxygen atoms coordinating Rh and the latter's two CO ligands; ReO_x remains in the immediate vicinity, with one of its O atoms coordinated to an Al_{III} site which is already hydroxylated. Therefore, the enhanced metal-to-ligand π back-donation should be attributed to a smaller energy gap between the π -donating d-orbitals of Rh and the unoccupied 2 π^* orbitals of CO. The mechanism via which this energy gap can be reduced involves ligand-to-metal π -donation, which raises those Rh d-orbitals that participate in metal-to-ligand π back-donation. The surface oxygen ligands are good π -donors, and their ligand field becomes stronger as their basicity increases. Table S4.2 shows the Bader partial charges on the surface oxygen ligands for all catalyst models considered. On the hydroxylated surface, Rh/2.9ReO₄-[Al₂O₃·H₂O](110), these charges have values in the range of −1.54e, which is a notable increase in the negative charge relative to the corresponding dry surface, Rh/2.9ReO₄-Al₂O₃(110), where these charges are in the range of −1.47e. The reason these surface O atoms carry more negative charge is that, while on the dry surface ReO_x is coordinated to a defect Al_{III} site that can readily accept electron density, on the wet surface this site is hydroxylated and the extra charge from ReO_x is delocalized over the surface O atoms in the vicinity, making them more basic (viz., stronger π -donors).

- A third interesting difference between the dry and wet (110) facets of the support is that although Rh in Rh(CO)₂/[Al₂O₃·H₂O](110) is in the +1 oxidation state (partial charge, +0.63e, and magnetic moment, 0

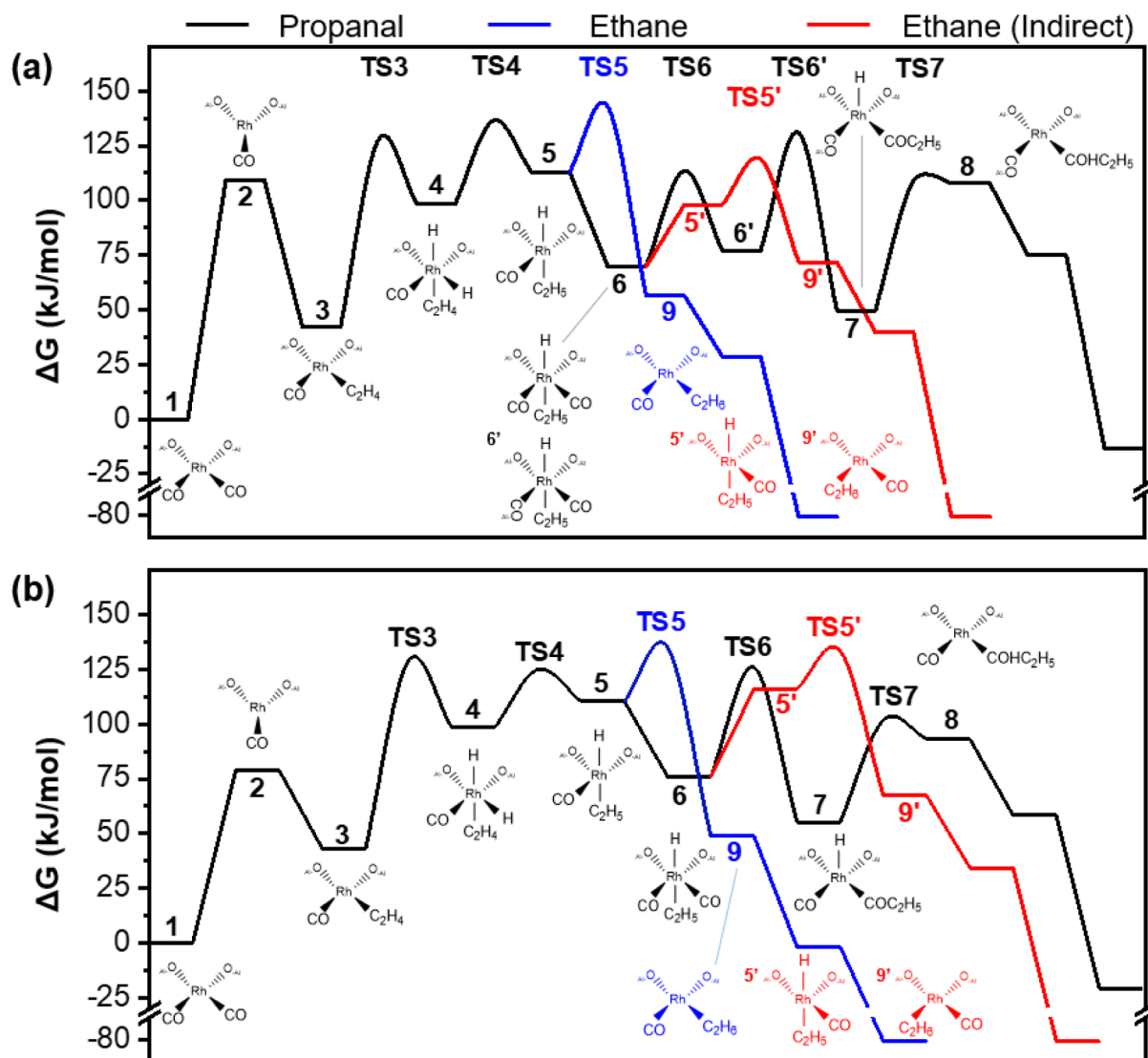


Figure 7. Free-energy profiles of ethylene hydroformylation (black line) and hydrogenation (blue or red line) on Rh/Al₂O₃ (a) and Rh/2.9ReO₄-Al₂O₃ (b). Free-energy values of all intermediates and transition states are provided in Table 2. (Energies in kJ/mol; $T = 423$ K.)

We have performed microkinetic analysis to assess the proposed mechanisms by comparing with the kinetic studies of Ro et al.¹² (see Section 2.3). Reaction path analysis for Rh/Al₂O₃(110) shows that only 9% of the reactive flux yields propanal while 91% produces ethane. These selectivity values are in satisfactory agreement with the experimental ones of 20 and 80%, respectively (Table 3).¹² Using the normalized rate of change of the selectivity with respect to the rate constants of the elementary steps, we determined that the selectivity for propanal is controlled by the CO insertion to the Rh–ethyl bond ($6' \rightarrow 7$), with a control coefficient of 0.86 (Table S1.4). This competes with the isomerization step $6 \rightarrow 5'$ that leads to ethane with a selectivity control coefficient of -0.67 .

On Rh/Al₂O₃(110), sensitivity analysis of the rate of propanal formation via the mechanism we proposed above showed that the catalyst turnover is limited by the CO insertion into the Rh–ethyl bond ($6' \rightarrow 7$), that is, the same step that controls the selectivity (Table S1.4). The respective apparent activation energy obtained from the microkinetic model is 62 kJ/mol (Figure S1.1), which compares favorably with the experimental value of 48 kJ/mol. The partial reaction orders with respect to C₂H₄ and H₂, 0.92 and 0.81, respectively

(Figure S1.2), are also in satisfactory agreement with the respective experimental values of 0.81 and 0.66. The near-first-order kinetics in the reactants are consistent with the low thermodynamic stability of the reaction intermediates, which is manifested in the low surface coverage in the reactants (Table S1.5). The careful tuning of the CO pressure is necessary as the first step of the reaction (catalyst activation) is inhibited by high CO pressure but the fifth step requires CO coordination to facilitate the insertion step, which as we noted earlier occurs readily only when Rh is octahedrally coordinated. In our microkinetic model, this is manifested in the negative reaction order (-0.14) with respect to CO.

Of the two hydrogenation pathways to ethane, the indirect one that proceeds via the CO isomerization step and intermediate $5'$ contributes 70% of the reactive flux (Figure 8). The rate of hydrogenation is controlled by the ethylene addition into the Rh–H bond ($4 \rightarrow 5$). Despite the 90% selectivity for hydrogenation on Rh/Al₂O₃(110), the model-predicted apparent activation energy of 117 kJ/mol is greater than that for hydroformylation by ca. 55 kJ/mol (Table 2). This relationship between the apparent activation energies of the two reactions is in agreement with the kinetic studies of Ro

Table 2. Relative Free Energies of Intermediates and Transition States Corresponding to the Profiles Shown in Figure 7^a

intermediate/transition state	Gibbs energy (kJ/mol)	
	Rh/Al ₂ O ₃	Rh/2.9ReO ₄ -Al ₂ O ₃
1	Rh(CO) ₂	0
2	Rh(CO)	109
3	Rh(CO)(C ₂ H ₄)	42
(3 → 4)	H ₂ dissociation	128
4	HRh(CO)(C ₂ H ₄)(H)	98
(4 → 5)	C ₂ H ₄ insertion	136
5	HRh(CO)(C ₂ H ₅)	113
6	HRh(CO) ₂ (C ₂ H ₅)	70
(6 → 6')	CO rearrangement	113
6'	HRh(CO) ₂ (C ₂ H ₅)	77
(6* → 7)	CO insertion	131
7	HRh(CO)(C ₃ H ₅ O)	50
(7 → 8)	C ₃ H ₆ O elimination	109
8	Rh(CO)(C ₃ H ₆ O)	108
(5 → 9)	C ₂ H ₆ elimination	143
9	Rh(CO)(C ₂ H ₆)	56
5'	HRh(C ₂ H ₅)(CO)	98
(5' → 9')	C ₂ H ₆ elimination	119
9'	Rh(C ₂ H ₆)(CO)	72

^aEnergies in kJ/mol; T = 423 K.

et al.,¹² who reported 48 kJ/mol for the hydroformylation and 110 kJ/mol for the hydrogenation. The hydrogenation partial reaction orders with respect to C₂H₄ and H₂ are the same as for hydroformylation. However, we see more potent inhibition by CO, with a partial order in CO of −0.63, which is in qualitative agreement with the experimental observations. The reason for this difference is that, in addition to the requisite CO dissociation that activates the catalyst and allows ethylene coordination, on the dominant hydrogenation pathway 6 → 5' → 9', the H and ethyl ligands are trans to each other (6) and for the ethyl addition to happen one of two CO ligands must desorb, so that the H and ethyl can rearrange into a cis conformation.

On Rh/2.9ReO₄-Al₂O₃(110), there is zero flux through the indirect hydrogenation pathway 6 → 5' → 9' (Figure 8) that contributes to the high ethane selectivity on Rh/Al₂O₃(110) because the ReO_x in the vicinity of Rh sterically impedes the 5 to 5' isomerization. When this isomerization channel is open, as in the case of Rh/Al₂O₃(110), the hydrogenation is controlled by the ethylene insertion into the Rh–H bond, but when it is closed, the turnover rate is determined by the final σ-type metathesis. As a result, the selectivity for propanal grows to 46% and that for ethane drops to 54%, which is in good agreement with the respective experimental values of 44

and 56%. There is also a change in the propanal formation rate- and selectivity-determining steps, from the CO insertion to the coordination of the second CO ligand. This is a direct consequence of the weaker CO binding to Rh, which keeps Rh from assuming the octahedral geometry that facilitates CO insertion toward the Rh–acyl complex. On Rh/2.9ReO₄-Al₂O₃(110), the hydroformylation apparent activation energy is lower than on Rh/Al₂O₃(110) by 6 kJ/mol (56 kJ/mol), which compares favorably with the experimental value of 49 kJ/mol. The predicted hydrogenation apparent activation energy of 91 kJ/mol is also in good agreement with the experimental value of 103 kJ/mol. Both the hydroformylation and the hydrogenation are first order in ethane and H₂, but the CO inhibition of the former is much weaker, with a negative partial order of −0.08 compared to −1.07 of the latter (Table 3). This is in qualitative agreement with the experiment.

Overall, the proposed mechanisms can reproduce most aspects of the kinetics of ethylene hydroformylation/hydrogenation by atomically dispersed Rh and Rh–ReO_x pairs on alumina. The most significant disagreement between our models and the experimental study of Ro et al.¹² is in the degree of CO inhibition, which our models consistently underpredict. We believe this is due to two related reasons: (a) as we noted earlier, the surface restructuring energy associated with CO coordination to Rh hints at an activated process. However, because we were unable to locate a transition state and obtain an accurate activation barrier, we modeled CO coordination as a non-activated process. (b) We were not able to locate the 5 → 5' isomerization transition state and thus modeled it as a consecutive, CO coordination-dissociation process.

In light of the microkinetic analysis, we can explain why the hydrogenation apparent activation energy is higher than that of the hydroformylation even though the selectivity for the former reaction is higher. The hydrogenation is thermodynamically more favorable than the hydroformylation and this intrinsically drives the selectivity. On Rh/Al₂O₃, the hydrogenation is rate-controlled by the hydrometalation step, which is common to both reactions. The only way to kinetically bias the reaction against hydrogenation is to increase the rate of conversion of 6 to 7, namely, to increase the rate of the CO insertion, which is exactly the reason the latter turns out to be the step that controls the hydroformylation rate (and selectivity). The associated activation energy is, however, lower than that of the hydrometalation step, as can be seen from the energy profile in Figure 7a. On Rh/2.9ReO₄-Al₂O₃, the ReO_x promoter shuts down the indirect pathway and the point at which the reaction can be now kinetically biased in favor of the hydroformylation is when intermediate 5 binds a second CO ligand (5 → 6). As we described earlier, this is the reason the hydroformylation rate-limiting step switches from

Table 3. Kinetic Parameters for Ethylene Hydroformylation and Hydrogenation on Rh/Al₂O₃ and Rh/2.9ReO₄-Al₂O₃ from Microkinetic Modeling and Experimental Literature¹²

		selectivity (%)	apparent activation energy (kJ/mol)	reaction order		
				CO	H ₂	C ₂ H ₄
Rh	propanal	9/20 ^a	62/48 ^a	−0.14/−0.70 ^a	0.80/0.66 ^a	0.92/0.81 ^a
	ethane	91/80 ^a	117/110 ^a	−0.63/−1.41 ^a	0.80/0.86 ^a	0.92/1.11 ^a
Rh/2.9ReO ₄	propanal	46/44 ^a	56/49 ^a	−0.08/−0.40 ^a	0.99/0.76 ^a	0.99/1.03 ^a
	ethane	54/56 ^a	90/102 ^a	−1.07/−1.00 ^a	0.99/0.89 ^a	0.99/1.03 ^a

^aExperimental data from ref 12.

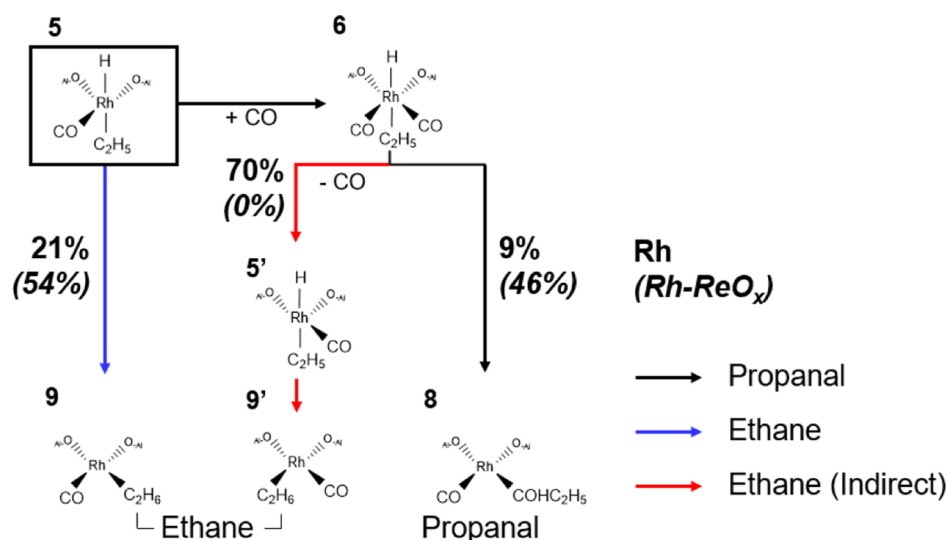


Figure 8. Reaction path analysis of Rh/Al₂O₃ (top) and Rh/2.9ReO₄-Al₂O₃ (bottom) for propanal (black) and ethane (blue and red) production. Numbers indicate incoming flux in percentage.

the acylation step to the CO coordination ($5 \rightarrow 6$). Once again, the associated activation barrier is lower than that for hydrogenation.

4. CONCLUSIONS

We have used DFT calculations and microkinetic modeling to develop and analyze the mechanisms of ethylene hydroformylation and hydrogenation by atomically dispersed Rh and Rh-ReO_x pairs on γ -Al₂O₃(110) and to elucidate the role of ReO_x in promoting the selectivity of Rh for hydroformylation.

We established that Rh(CO)₂ coordinated to two surface oxygen atoms is the most stable pre-catalyst complex, in a 16-electron configuration that assumes the square-planar geometry. Both on the dry and hydroxylated γ -Al₂O₃(110) surfaces, and independently of the Re loading, Rh is oxidized to the +1 state upon coordination of the two CO ligands. The Rh-CO coordinative bonds weaken with increasing ReO_x loading, but our analysis showed no evidence of Rh becoming more cationic. On dry γ -Al₂O₃(110), vibrational analysis showed that the weakening of the Rh-CO bond is accompanied by a blue shift in the CO stretching vibrations due to weaker metal-to-ligand π back-donation, confirming the conclusions of Ro et al.¹² However, we demonstrated that this correlation is not generally true because, on the hydroxylated surface, the CO vibrations were significantly red-shifted. Because the dry Al₂O₃(110) surface provided the most similar Rh(CO)₂ frequency behavior to the experimental systems, it was used as the model system for the mechanistic development studies on Rh/*n*ReO_x-Al₂O₃(110) for *n* = 0 and *n* = 2.9 wt % ReO_x loading. Activation of the catalyst requires the dissociation of one of Rh's CO ligands, which is more facile in the presence of ReO_x.

We examined numerous catalytic pathways for ethylene hydroformylation and hydrogenation and ranked them by their respective reaction fluxes using microkinetic modeling and reaction path analysis. The proposed dominant catalytic pathways were able to reproduce all the major trends in selectivity and kinetic parameters reported by Ro et al.¹² The propanal pathway, in particular, differs from the homogeneous one in that the H₂ coordination occurs at the top of the cycle right after ethylene coordination and is not oxidative, namely,

Rh remains in the +1 state. In the absence of the ReO_x promoter, the hydroformylation is controlled by the CO insertion into the Rh-ethyl bond and requires octahedrally coordinated Rh, namely, coordination of a second CO ligand prior to the acylation. In fact, owing to the weakening of the Rh-CO coordinative bond, the requisite second CO coordination becomes rate-limiting in the presence of ReO_x.

On the other hand, hydrogenation to ethane occurs prior to Rh assuming an octahedral geometry and is facilitated by the isomerization of the penta-coordinated Rh complex that changes the positions of the H and ethyl ligands relative to the single CO ligand of Rh. This is the dominant pathway on Rh/Al₂O₃(110). However, on Re/ReO_x-Al₂O₃(110), the promoter in the immediate vicinity of Rh impedes the aforementioned isomerization and effectively shuts down the major ethane catalytic pathway and promotes propanal formation.

■ ASSOCIATED CONTENT

Supporting Information

The Supporting Information is available free of charge at <https://pubs.acs.org/doi/10.1021/acscatal.1c00705>.

Additional DFT calculation details; charge density analysis; alternative hydroformylation and hydrogenation pathways; microkinetic model parameters and results; images of optimized intermediates; and coordinates of intermediates and transition states referenced in the main text (PDF)

Electronic energies and vibrational frequencies of all intermediates and transition states (ZIP)

■ AUTHOR INFORMATION

Corresponding Author

Stavros Caratzoulas — Catalysis Center for Energy Innovation, University of Delaware, Newark, Delaware 19716, United States; orcid.org/0000-0001-9599-4199; Email: cstavros@udel.edu

Authors

Seungyeon Lee — Department of Chemical and Biomolecular Engineering, University of Delaware, Newark, Delaware

19716, United States; Catalysis Center for Energy Innovation, University of Delaware, Newark, Delaware 19716, United States

Abhirup Patra – Catalysis Center for Energy Innovation, University of Delaware, Newark, Delaware 19716, United States

Phillip Christopher – Catalysis Center for Energy Innovation, University of Delaware, Newark, Delaware 19716, United States; Department of Chemical Engineering, University of California, Santa Barbara, Santa Barbara, California 93106, United States; orcid.org/0000-0002-4898-5510

Dionisios G. Vlachos – Department of Chemical and Biomolecular Engineering, University of Delaware, Newark, Delaware 19716, United States; Catalysis Center for Energy Innovation, University of Delaware, Newark, Delaware 19716, United States; orcid.org/0000-0002-6795-8403

Complete contact information is available at:
<https://pubs.acs.org/10.1021/acscatal.1c00705>

Notes

The authors declare no competing financial interest.

ACKNOWLEDGMENTS

This work was supported as part of the Catalysis Center for Energy Innovation, an Energy Frontier Research Center funded by the US Dept. of Energy, Office of Science, Office of Basic Energy Sciences under award number DE-SC0001004.

REFERENCES

- (1) Liu, J. Catalysis by Supported Single Metal Atoms. *ACS Catal.* **2017**, *7*, 34–59.
- (2) Yang, X.-F.; Wang, A.; Qiao, B.; Li, J.; Liu, J.; Zhang, T. Single-Atom Catalysts: A New Frontier in Heterogeneous Catalysis. *Acc. Chem. Res.* **2013**, *46*, 1740–1748.
- (3) Qiao, B.; Liang, J.-X.; Wang, A.; Xu, C.-Q.; Li, J.; Zhang, T.; Liu, J. J. Ultrastable Single-Atom Gold Catalysts with Strong Covalent Metal-Support Interaction (CMSI). *Nano Res.* **2015**, *8*, 2913–2924.
- (4) Gu, X.-K.; Qiao, B.; Huang, C.-Q.; Ding, W.-C.; Sun, K.; Zhan, E.; Zhang, T.; Liu, J.; Li, W.-X. Supported Single Pt1/Au1 Atoms for Methanol Steam Reforming. *ACS Catal.* **2014**, *4*, 3886–3890.
- (5) Vilé, G.; Albani, D.; Nachtegaal, M.; Chen, Z.; Dontsova, D.; Antonietti, M.; López, N.; Pérez-Ramírez, J. A Stable Single-Site Palladium Catalyst for Hydrogenations. *Angew. Chem., Int. Ed.* **2015**, *54*, 11265–11269.
- (6) Lang, R.; Li, T.; Matsumura, D.; Miao, S.; Ren, Y.; Cui, Y.-T.; Tan, Y.; Qiao, B.; Li, L.; Wang, A.; Wang, X.; Zhang, T. Hydroformylation of Olefins by a Rhodium Single-Atom Catalyst with Activity Comparable to RhCl(PPh₃)₃. *Angew. Chem., Int. Ed.* **2016**, *55*, 16054–16058.
- (7) Lu, Y.; Wang, J.; Yu, L.; Kovarik, L.; Zhang, X.; Hoffman, A. S.; Gallo, A.; Bare, S. R.; Sokaras, D.; Kroll, T.; Dagle, V.; Xin, H.; Karim, A. M. Identification of the Active Complex for CO Oxidation over Single-Atom Ir-on-MgAl₂O₄ Catalysts. *Nat. Catal.* **2019**, *2*, 149–156.
- (8) Zhang, Z.; Zhu, Y.; Asakura, H.; Zhang, B.; Zhang, J.; Zhou, M.; Han, Y.; Tanaka, T.; Wang, A.; Zhang, T.; Yan, N. Thermally Stable Single Atom Pt/m-Al₂O₃ for Selective Hydrogenation and CO Oxidation. *Nat. Commun.* **2017**, *8*, 16100.
- (9) Kropp, T.; Lu, Z.; Li, Z.; Chin, Y.-H. C.; Mavrikakis, M. Anionic Single-Atom Catalysts for CO Oxidation: Support-Independent Activity at Low Temperatures. *ACS Catal.* **2019**, *9*, 1595–1604.
- (10) Hanf, S.; Alvarado Rupflin, L.; Gläser, R.; Schunk, S. Current State of the Art of the Solid Rh-Based Catalyzed Hydroformylation of Short-Chain Olefins. *Catalysts* **2020**, *10*, 510.
- (11) Franke, R.; Selent, D.; Börner, A. Applied Hydroformylation. *Chem. Rev.* **2012**, *112*, 5675–5732.
- (12) Ro, I.; Xu, M.; Graham, G. W.; Pan, X.; Christopher, P. Synthesis of Heteroatom Rh–ReOx Atomically Dispersed Species on Al₂O₃ and Their Tunable Catalytic Reactivity in Ethylene Hydroformylation. *ACS Catal.* **2019**, *9*, 10899–10912.
- (13) Heck, R. F.; Breslow, D. S. The Reaction of Cobalt Hydrotetracarbonyl with Olefins. *J. Am. Chem. Soc.* **1961**, *83*, 4023–4027.
- (14) van Leeuwen, P. W. M. N.; Casey, C. P.; Whiteker, G. T. In *Rhodium Catalyzed Hydroformylation*; van Leeuwen, P. W. M. N., Claver, C., Eds.; Kluwer Academic Publishers: Boston, 2000.
- (15) Hebrard, F.; Kalck, P. Cobalt-Catalyzed Hydroformylation of Alkenes: Generation and Recycling of the Carbonyl Species, and Catalytic Cycle. *Chem. Rev.* **2009**, *109*, 4272–4282.
- (16) Watkins, A. L.; Landis, C. R. Origin of Pressure Effects on Regioselectivity and Enantioselectivity in the Rhodium-Catalyzed Hydroformylation of Styrene with (S,S,S)-BisDiazaphos. *J. Am. Chem. Soc.* **2010**, *132*, 10306–10317.
- (17) Huo, C.-F.; Li, Y.-W.; Beller, M.; Jiao, H. HCo(CO)₃-Catalyzed Propene Hydroformylation. Insight into Detailed Mechanism. *Organometallics* **2003**, *22*, 4665–4677.
- (18) Rush, L. E.; Pringle, P. G.; Harvey, J. N. Computational Kinetics of Cobalt-Catalyzed Alkene Hydroformylation. *Angew. Chem., Int. Ed.* **2014**, *53*, 8672–8676.
- (19) Gleich, D.; Hutter, J. Computational Approaches to Activity in Rhodium-Catalyzed Hydroformylation. *Chemistry* **2004**, *10*, 2435–2444.
- (20) Decker, S. A.; Cundari, T. R. DFT Study of the Ethylene Hydroformylation Catalytic Cycle Employing a HRh(PH₃)₂(CO) Model Catalyst. *Organometallics* **2001**, *20*, 2827–2841.
- (21) Jacobs, I.; de Bruin, B.; Reek, J. N. H. Comparison of the Full Catalytic Cycle of Hydroformylation Mediated by Mono- and Bis-Ligated Triphenylphosphine–Rhodium Complexes by Using DFT Calculations. *ChemCatChem* **2015**, *7*, 1708–1718.
- (22) Sparta, M.; Børve, K. J.; Jensen, V. R. Activity of Rhodium-Catalyzed Hydroformylation: Added Insight and Predictions from Theory. *J. Am. Chem. Soc.* **2007**, *129*, 8487–8499.
- (23) Navidi, N.; Thybaut, J. W.; Marin, G. B. Experimental Investigation of Ethylene Hydroformylation to Propanal on Rh and Co Based Catalysts. *Appl. Catal., A* **2014**, *469*, 357–366.
- (24) Navidi, N.; Marin, G. B.; Thybaut, J. W. A Single-Event Microkinetic Model for Ethylene Hydroformylation to Propanal on Rh and Co Based Catalysts. *Appl. Catal., A* **2016**, *524*, 32–44.
- (25) Xie, Z.; Xu, Y.; Xie, M.; Chen, X.; Lee, J. H.; Stavitski, E.; Kattel, S.; Chen, J. G. Reactions of CO₂ and Ethane Enable CO Bond Insertion for Production of C₃ Oxygenates. *Nat. Commun.* **2020**, *11*, 1887.
- (26) Huang, N.; Liu, B.; Lan, X.; Wang, T. Insights into the Bimetallic Effects of a RhCo Catalyst for Ethene Hydroformylation: Experimental and DFT Investigations. *Ind. Eng. Chem. Res.* **2020**, *59*, 18771–18780.
- (27) Wang, L.; Zhang, W.; Wang, S.; Gao, Z.; Luo, Z.; Wang, X.; Zeng, R.; Li, A.; Li, H.; Wang, M.; Zheng, X.; Zhu, J.; Zhang, W.; Ma, C.; Si, R.; Zeng, J. Atomic-Level Insights in Optimizing Reaction Paths for Hydroformylation Reaction over Rh/CoO Single-Atom Catalyst. *Nat. Commun.* **2016**, *7*, 14036.
- (28) Liu, B.; Huang, N.; Wang, Y.; Lan, X.; Wang, T. Promotion of Inorganic Phosphorus on Rh Catalysts in Styrene Hydroformylation: Geometric and Electronic Effects. *ACS Catal.* **2021**, *11*, 1787–1796.
- (29) Amsler, J.; Sarma, B. B.; Agostini, G.; Prieto, G.; Plessow, P. N.; Studt, F. Prospects of Heterogeneous Hydroformylation with Supported Single Atom Catalysts. *J. Am. Chem. Soc.* **2020**, *142*, 5087–5096.
- (30) Krokidis, X.; Raybaud, P.; Gobichon, A.-E.; Rebours, B.; Euzen, P.; Toulhoat, H. Theoretical Study of the Dehydration Process of Boehmite to γ -Alumina. *J. Phys. Chem. B* **2001**, *105*, 5121–5130.
- (31) Digne, M.; Sautet, P.; Raybaud, P.; Euzen, P.; Toulhoat, H. Use of DFT to Achieve a Rational Understanding of Acid–Basic Properties of γ -Alumina Surfaces. *J. Catal.* **2004**, *226*, 54–68.

- (32) Nortier, P.; Fourre, P.; Saad, A. B. M.; Saur, O.; Lavalley, J. C. Effects of Crystallinity and Morphology on the Surface Properties of γ -Alumina. *Appl. Catal.* **1990**, *61*, 141–160.
- (33) Digne, M.; Sautet, P.; Raybaud, P.; Euzen, P.; Toulhoat, H. Hydroxyl Groups on γ -Alumina Surfaces: A DFT Study. *J. Catal.* **2002**, *211*, 1–5.
- (34) Lwin, S.; Keturakis, C.; Handzlik, J.; Sautet, P.; Li, Y.; Frenkel, A. I.; Wachs, I. E. Surface ReOx Sites on Al_2O_3 and Their Molecular Structure–Reactivity Relationships for Olefin Metathesis. *ACS Catal.* **2015**, *5*, 1432–1444.
- (35) Perdew, J. P.; Burke, K.; Ernzerhof, M. Generalized Gradient Approximation Made Simple. *Phys. Rev. Lett.* **1997**, *78*, 1396.
- (36) Grimme, S.; Antony, J.; Ehrlich, S.; Krieg, H. A Consistent and Accurate Ab Initio Parametrization of Density Functional Dispersion Correction (DFT-D) for the 94 Elements H–Pu. *J. Chem. Phys.* **2010**, *132*, 154104.
- (37) Kresse, G.; Joubert, D. From Ultrasoft Pseudopotentials to the Projector Augmented-Wave Method. *Phys. Rev. B: Condens. Matter Phys.* **1999**, *59*, 1758–1775.
- (38) Blöchl, P. E. Projector Augmented-Wave Method. *Phys. Rev. B: Condens. Matter Phys.* **1994**, *50*, 17953–17979.
- (39) Sheppard, D.; Terrell, R.; Henkelman, G. Optimization Methods for Finding Minimum Energy Paths. *J. Chem. Phys.* **2008**, *128*, 134106.
- (40) Sheppard, D.; Xiao, P.; Chemelewski, W.; Johnson, D. D.; Henkelman, G. A Generalized Solid-State Nudged Elastic Band Method. *J. Chem. Phys.* **2012**, *136*, 074103.
- (41) Kresse, G.; Furthmüller, J. Efficiency of Ab-Initio Total Energy Calculations for Metals and Semiconductors Using a Plane-Wave Basis Set. *Comput. Mater. Sci.* **1996**, *6*, 15–50.
- (42) Kresse, G.; Furthmüller, J. Efficient Iterative Schemes for Ab Initio Total-Energy Calculations Using a Plane-Wave Basis Set. *Phys. Rev. B: Condens. Matter Phys.* **1996**, *54*, 11169–11186.
- (43) Bader, R. F. W. A Quantum Theory of Molecular Structure and Its Applications. *Chem. Rev.* **1991**, *91*, 893–928.
- (44) Henkelman, G.; Arnaldsson, A.; Jónsson, H. A Fast and Robust Algorithm for Bader Decomposition of Charge Density. *Comput. Mater. Sci.* **2006**, *36*, 354–360.
- (45) Mallikarjun Sharada, S.; Bligaard, T.; Luntz, A. C.; Kroes, G.-J.; Nørskov, J. K. SBH10: A Benchmark Database of Barrier Heights on Transition Metal Surfaces. *J. Phys. Chem. C* **2017**, *121*, 19807–19815.
- (46) Tameh, M. S.; Dearden, A. K.; Huang, C. Accuracy of Density Functional Theory for Predicting Kinetics of Methanol Synthesis from CO and CO_2 Hydrogenation on Copper. *J. Phys. Chem. C* **2018**, *122*, 17942–17953.
- (47) Zhang, T.; Yang, X.; Ge, Q. Surface Chemistry and Reactivity of α - MoO_3 toward Methane: A SCAN-Functional Based DFT Study. *J. Chem. Phys.* **2019**, *151*, 044708.
- (48) Guner, V.; Khuong, K. S.; Leach, A. G.; Lee, P. S.; Bartberger, M. D.; Houk, K. N. A Standard Set of Pericyclic Reactions of Hydrocarbons for the Benchmarking of Computational Methods: The Performance of Ab Initio, Density Functional, CASSCF, CASPT2, and CBS-QB3 Methods for the Prediction of Activation Barriers, Reaction Energetics, and Transition State Geometries. *J. Phys. Chem. A* **2003**, *107*, 11445–11459.
- (49) Kanai, Y.; Wang, X.; Selloni, A.; Car, R. Testing the TPSS Meta-Generalized-Gradient-Approximation Exchange-Correlation Functional in Calculations of Transition States and Reaction Barriers. *J. Chem. Phys.* **2006**, *125*, 234104.
- (50) Ishikawa, A.; Tateyama, Y. Hybrid Functional Study of H-Abstraction from Methane by Li-Doped, Pristine and Stepped $\text{MgO}(100)$ and $\text{MgO}(110)$ Surfaces. *Catal. Lett.* **2021**, *151*, 627–633.
- (51) Coltrin, M. E.; Kee, R. J.; Rupley, F. M.; Meeks, E. SURFACE CHEMKIN-III: A Fortran Package for Analyzing Heterogeneous Chemical Kinetics at a Solid-Surface–Gas-Phase Interface, 1996.
- (52) Lym, J.; Wittreich, G. R.; Vlachos, D. G. A Python Multiscale Thermochemistry Toolbox (PMuTT) for Thermochemical and Kinetic Parameter Estimation. *Comput. Phys. Commun.* **2020**, *247*, 106864.
- (53) Chia, M.; Pagán-Torres, Y. J.; Hibbitts, D.; Tan, Q.; Pham, H. N.; Datye, A. K.; Neurock, M.; Davis, R. J.; Dumesic, J. A. Selective Hydrogenolysis of Polyols and Cyclic Ethers over Bifunctional Surface Sites on Rhodium–Rhenium Catalysts. *J. Am. Chem. Soc.* **2011**, *133*, 12675–12689.
- (54) Hoffman, R. *Solids and Surfaces: A Chemist's View of Bonding in Extended Structures*; Wiley, 1989.
- (55) Raatz, F.; Salahub, D. R. Chemisorption and Magnetism: CO on Ni Clusters. *Surf. Sci. Lett.* **1984**, *146*, L609–L615.
- (56) Andzelm, J.; Salahub, D. R. Chemisorption of CO on $\text{Pd}(100)$: An Lcgto-Lsd Cluster Study. *Int. J. Quantum Chem.* **1986**, *29*, 1091–1104.
- (57) Bare, S. R.; Kelly, S. D.; Vila, F.; Karapetrova, E.; Kas, J.; Mickelson, G. E.; Modica, F. S.; Yang, N.; Rehr, J. J. Experimental (XAS, STEM, TPR, and XPS) and Theoretical (DFT) Characterization of Supported Rhenium Catalysts. *J. Phys. Chem. C* **2011**, *115*, 5740–5755.
- (58) Lacheen, H. S.; Cordeiro, P. J.; Iglesia, E. Isolation of Rhenium and ReOx Species within ZSM5 Channels and Their Catalytic Function in the Activation of Alkanes and Alkanols. *Chem.—Eur. J.* **2007**, *13*, 3048–3057.
- (59) Huang, L.; Xu, Y.; Guo, W.; Liu, A.; Li, D.; Guo, X. Study on Catalysis by Carbonyl Cluster-Derived SiO_2 -Supported Rhodium for Ethylene Hydroformylation. *Catal. Lett.* **1995**, *32*, 61–81.
- (60) Basu, P.; Panayotov, D.; Yates, J. T. Rhodium–Carbon Monoxide Surface Chemistry: The Involvement of Surface Hydroxyl Groups on Alumina and Silica Supports. *J. Am. Chem. Soc.* **1988**, *110*, 2074–2081.
- (61) Miessler, G.; Fischer, P.; Tarr, D. *Inorganic Chemistry*, 5th ed.; Pearson, 2013.
- (62) Dunnington, B. D.; Schmidt, J. R. Generalization of Natural Bond Orbital Analysis to Periodic Systems: Applications to Solids and Surfaces via Plane-Wave Density Functional Theory. *J. Chem. Theory Comput.* **2012**, *8*, 1902–1911.